FERMILAB-PUB-10-067-T

Draft version January 26, 2010
Preprint typeset using LaTeX style emulateapj v. 04/20/08

arXiv:1001.2324v2 [astro-ph.CO] 25 Jan 2010

A NEW STATISTIC FOR ANALYZING BARYON ACOUSTIC OSCILLATIONS

X. Xu[1], M. White[2,3], N. Padmanabhan[4], D. J. Eisenstein[1], J. Eckel[1], K. Mehta[1], M. Metchnik[1], P. Pinto[1], H.-J. Seo[5]

Draft version January 26, 2010

ABSTRACT

We introduce a new statistic $\omega_\ell(r_s)$ for measuring and analyzing large-scale structure and particularly the baryon acoustic oscillations. $\omega_\ell(r_s)$ is a band-filtered, configuration space statistic that is easily implemented and has advantages over the traditional power spectrum and correlation function estimators. Unlike these estimators, $\omega_\ell(r_s)$ can localize most of the acoustic information into a single dip at the acoustic scale while also avoiding sensitivity to the poorly constrained large scale power (i.e., the integral constraint) through the use of a localized and compensated filter. It is also sensitive to anisotropic clustering through pair counting and does not require any binning. We measure the shift in the acoustic peak due to nonlinear effects using the monopole $\omega_0(r_s)$ derived from subsampled dark matter catalogues as well as from mock galaxy catalogues created via halo occupation distribution (HOD) modeling. All of these are drawn from 44 realizations of 1024^3 particle dark matter simulations in a $1h^{-1}$ Gpc box at z=1. We compare these shifts with those obtained from the power spectrum and conclude that the results agree. This indicates that any distance measurements obtained from $\omega_0(r_s)$ and $P(k)$ will be consistent with each other. We also show that it is possible to extract the same amount of acoustic information using either $\omega_0(r_s)$ or $P(k)$ from equal volume surveys.

Subject headings: distance scale — cosmological parameters — large-scale structure of universe — methods: N-body simulations — cosmology: theory

1. INTRODUCTION

Baryon acoustic oscillations (BAOs) are relic imprints on the baryon distribution left behind by the interaction between radiation and matter in the primordial universe. The large amount of radiation pressure due to high temperatures in the early universe pushed matter apart as it congregated under the influence of gravity. Oscillating sound waves were set up in the primordial plasma due to these two competing effects (Peebles & Yu 1970; Sunyaev & Zeldovich 1970; Bond & Efstathiou 1984; Holtzman 1989; Hu & Sugiyama 1996; Hu & White 1996; Eisenstein & Hu 1998). The distance traveled by these sound waves before recombination is about 150 comoving Mpc and is known as the acoustic scale. When the photons stream off, the baryons are deposited at these characteristic separations and hence we would expect excesses with this separation in the baryon distribution today. This characteristic scale makes for a very useful standard ruler (Eisenstein & Hu 1998; Eisenstein et al. 1998; Eisenstein 2003; Blake & Glazebrook 2003; Hu & Haiman 2003; Linder 2003; Seo & Eisenstein 2003; Matsubara 2004; Amendola et al. 2005).

As the universe evolves, primordial density perturbations begin to grow nonlinearly, especially on small scales (Jain & Bertschinger 1994; Meiksin et al. 1999; Meiksin & White 1999; Scoccimarro et al. 1999). This causes the acoustic scale to become slightly shifted from its predicted linear theory position (Seo & Eisenstein 2005; Huff et al. 2007; Ma 2007; Angulo et al. 2008; Crocce & Scoccimarro 2008; Sanchez et al. 2008; Seo et al. 2008; Smith et al. 2008; Padmanabhan & White 2009). One must calibrate this shift before the acoustic scale can be used as a high precision standard ruler.

Previous calibrations and other analyses of the acoustic signature have been conducted using the traditional power spectrum and correlation function methods. Although analytically they are both perfectly adequate, the estimators used to derive them from simulations and observational data are subject to numerous difficulties.

The largest survey scales are always poorly constrained due to effects such as the integral constraint making it a challenge to estimate the correlation function $\xi(r)$ accurately at these scales. The integral constraint arises due to the fact that we do not know the cosmic number density of any population of mass tracers (de Lapparent et al. 1988; Baumgart & Fry 1991; Peacock & Nicholson 1991; Hamilton 1993). Current techniques used to estimate $\xi(r)$ (Peebles 1973; Sharp 1979; Hewett 1982; Blanchard & Alimini 1988; Landy & Szalay 1993; Hamilton 1993) take the number density of tracers in the survey volume to be the true number density. This assumption effectively ignores all power at scales larger than the survey size while simultaneously increasing the correlation between scales smaller than the survey size which causes the off-diagonal covariance matrix terms to be larger than they would be otherwise.

Limited survey volume and awkward survey boundaries are the major concerns when trying to estimate the power spectrum $P(k)$. Typically, the

[1] Steward Observatory, University of Arizona, 933 N. Cherry Ave., Tucson, AZ 85121; xxu@as.arizona.edu
[2] Departments of Physics and Astronomy, University of California, Berkeley, CA 94720
[3] Lawrence Berkeley National Laboratory, 1 Cyclotron Road, Berkeley, CA
[4] Department of Physics, Yale University, New Haven, CT 06511
[5] Center for Particle Astrophysics, Fermi National Accelerator Laboratory, P.O. Box 500, Batavia, IL 60510-5011

Operated by Fermi Research Alliance, LLC under Contract No. De-AC02-07CH11359 with the United States Department of Energy.

measured power spectrum is a convolution of the window function, the Fourier transform of the selection function of the survey, and the underlying true power spectrum (Feldman et al. 1994; Park et al. 1992; Baumgart & Fry 1991; Peacock & Nicholson 1991; Kaiser & Peacock 1991). Therefore, these $P(k)$ estimators are biased. In the limit of infinite volume, the window function should be a delta function. However, real surveys have finite volume and hence the window function has a finite albeit very small width. This induces an artificial smoothing at small separations in k when attempting to deconvolve the window function from the observed density field.

Estimating $\xi(r)$ and $P(k)$ also requires the binning of data. When any binning process is invoked, one must carefully define any averaging used to derive the value in each bin. To reduce these errors, bin sizes are made smaller which increases the dimensionality of the covariance matrix, making it even more difficult to estimate. Also, survey boundaries need to be addressed with special care.

In the study of large scale structure, we are also interested in any anisotropies in the distribution of objects. These can result from the bulk motions of objects (Peebles 1980; Davis & Peebles 1983; Kaiser 1987) as well as assumed models for the Hubble parameter $H(z)$ and the angular diameter distance $D_A(z)$ while calculating object separations along the line of sight (LOS) and transverse directions respectively. Since, at large scales we would expect the distribution to be isotropic, any anisotropy can be deconstructed into velocity field information which in turn provides us with constraints on Ω_m (Kaiser 1987; Hamilton 1998; Peacock et al. 2001; Hawkins et al. 2003; Tegmark et al. 2002; Zehavi et al. 2002) and the derivative of the growth function $f = d\ln D/d\ln a$ (Song & Percival 2008; Percival & White 2009; White et al. 2009). After modeling these anisotropies, any residual anisotropies can be used to constrain $D_A(z)H(z)$ (Alcock & Paczynski 1979). If our assumed $H(z)$ or $D_A(z)$ models are incorrect then the distribution of objects will still appear anisotropic after the bulk motion effects are removed. The magnitude of this residual anisotropy can be used to infer the true underlying cosmology (Padmanabhan & White 2008; Okumura et al. 2008).

Anisotropic information can be extracted from the redshift-space correlation function and to a lesser extent from the redshift space power spectrum (Szalay et al. 1998). If one imagines a wide angle survey, $P(k)$ estimators that rely on a Fourier transform from a Cartesian grid will suffer because an arbitrary wave vector ($\vec{k}$) will not necessarily be parallel to the LOS (Cole et al. 1994, 1995; Zaroubi & Hoffman 1995; Szapudi 2004). This means that each $\vec{k}$ mode will contain information about both the LOS and transverse distributions. After averaging to obtain the spherically averaged power spectrum, any anistropies in the distribution of survey objects will have been erased. Instead of taking a spherical average, one can also analyze the full 3D $P(\vec{k})$ through Legendre decomposition into radial and angular components. However, an infinite sum is required and applicability is limited to the linear regime (Heavens & Taylor 1995; Percival et al. 2004). Pair count estimators for $\xi(r)$, on the other hand, record the distribution of tracers in both the LOS and transverse directions accurately. Statistics sensitive to anisotropic clustering are desirable as they offer us a means to probe the underlying cosmology.

Ideally, we would also like the acoustic information to be localized into a single feature at the acoustic scale to simplify analysis. This is true for $\xi(r)$ but not for $P(k)$, which has oscillatory acoustic features.

Although all of the above mentioned disadvantages of $\xi(r)$ and $P(k)$ are minor, it is still beneficial to derive a new statistic that does away with as many of the above setbacks as possible. $\omega_\ell(r_s)$ is an example of such an alternative.

The organization of this paper will be as follows. In §2, we introduce $\omega_\ell(r_s)$, including its properties and computation. In §3, we describe the simulations, halo occupation models and analysis methods we use to derive acoustic peak shifts through implementation of the monopole $\omega_0(r_s)$. We demonstrate the mutual consistency between the peak shifts measured from the same simulations using $\omega_0(r_s)$ and $P(k)$ in §4. This is indicative of the agreement we expect between distance measures from $\omega_0(r_s)$ and $P(k)$. We also show that with a reasonable finite fitting range and our current choice of filter for computing $\omega_\ell(r_s)$, we can extract the same amount of acoustic information using either $\omega_0(r_s)$ or $P(k)$ from equal volume surveys. Finally, we state the main results of this paper in §5. Details of the matter and galaxy model $P(k)$ results discussed in this paper can be found in the companion papers Seo et al. (submitted) and Mehta et al. (in prep) respectively.

2. THE $\omega_\ell(r_s)$ STATISTIC

2.1. *Equations and Properties*

We expand the angle dependence of the power spectrum and correlation function out as a series of Legendre polynomials:

$$\xi(r, \hat{r}\cdot\hat{z}) \equiv \sum_\ell \xi_\ell(r) L_\ell(\hat{r}\cdot\hat{z}) \tag{1}$$

$$\Delta^2(k, \hat{k}\cdot\hat{z}) \equiv \frac{k^3 P(k,\mu)}{2\pi^2} = \sum_\ell \Delta^2_\ell(k) L_\ell(\mu) \tag{2}$$

so that

$$\xi_\ell(r) = i^\ell \int \frac{dk}{k}\, \Delta^2_\ell(k) j_\ell(kr) \tag{3}$$

where j_ℓ is the spherical Bessel function of order ℓ and L_ℓ is the Legendre polynomial of order ℓ.

Imagine we have a filter, $W_\ell(r,\mu,r_s) = W_\ell(r,r_s)L_\ell(\mu)$, which we take to be compact and compensated ($\int r^2\, dr\, W_\ell(r,r_s) = 0$) with a characteristic scale r_s. We define our statistic as the redshift-space correlation function, $\xi_s(r,\mu)$, convolved with the filter as a function of filtering scale r_s.

$$\omega_\ell(r_s) \equiv i^\ell \int d^3r\, \xi_s(r,\mu) W_\ell(r,r_s) L_\ell(\mu) \tag{4}$$

$$= \frac{4\pi i^\ell}{2\ell+1} \int r^2\, dr\, \xi_\ell(r) W_\ell(r,r_s) \tag{5}$$

$$= \int \frac{dk}{k}\, \Delta^2_\ell(k) \widetilde{W}_\ell(k,r_s) \tag{6}$$

with

$$\widetilde{W}_\ell(k, r_s) \equiv (-1)^\ell \frac{4\pi}{2\ell+1} \int r^2\, dr\; W_\ell(r, r_s) j_\ell(kr) \quad (7)$$

where the i^ℓ has been inserted for later convenience. By making the filter compensated, we reduce the sensitivity to the poorly constrained power at large scales and the dependence on the uncertain mean density in the sample. The correlation function is defined such that $\xi(r,\mu) + 1 \propto n^{-2}$ (Peebles 1980). Integrating the left-hand side against $W_\ell(r, r_s) L_\ell(\mu) d^3r$ results in $\omega_\ell(r_s)$ scaling directly with n^{-2} following equation (4). The constant term integrates to 0 as the filter is compensated. Hence, any uncertainty in n enters as a pure multiplicative offset in $\omega_\ell(r_s)$, which does not overwhelm the acoustic signature at large scales. This in essence, eliminates sensitivity to the integral constraint, which is a small effect to begin with. This feature of the filter also makes the statistic measured in different subvolumes of a survey more independent, an important feature as it makes internal error estimates from methods such as bootstrap or jackknife more robust (Padmanabhan et al. 2009).

Following Padmanabhan et al. (2007) we consider a low order, smooth compensated filter. For simplicity we assume W_ℓ is independent of ℓ, though we could of course choose different weights for each multipole[6]. In terms of $x \equiv (r/r_s)^3$, the filter

$$W(x) = (2x)^2 (1-x)^2 \left(\frac{1}{2} - x\right) \frac{1}{r_s^3} \quad (8)$$

satisfies $W(0) = W'(0) = W(1) = W'(1) = 0$ and $\int dx\, W(x) = 0$. The suggested form in configuration space (top panel of Figure 1) has a broad hump peaking at $r \simeq 0.65\, r_s$ that matches the width of the acoustic peak in $\xi(r)$ and a sharp (negative) spike at $0.9\, r_s$ of width $\mathcal{O}(10\%)$. This filter will smear a feature, such as the acoustic peak in $\xi(r)$, by very little which means that the acoustic information will be localized in $\omega_\ell(r_s)$, however, not as localized as in $\xi(r)$. Obviously, given sufficient signal-to-noise, measuring $\omega_\ell(r_s)$ for many r_s values would allow resolution in $\xi(r)$ even below the intrinsic width of $W(r/r_s)$ (see §2.3).

With this choice of W_ℓ the window function $\widetilde{W}_\ell$ can be computed analytically (see Appendix for numerical details) or numerically via fast Hankel transforms. We show $\widetilde{W}_\ell(kr_s)$ for $\ell = 0$, in the bottom panel of Figure 1. Since the filter is singly compensated, $\widetilde{W}_\ell \sim k^2$ as $k \to 0$, reflecting insensitivity to large scales. At small scales $\widetilde{W}_\ell(kr_s) \to \cos(kr_s)/(kr_s)^4$, a much more rapid convergence than evinced by the kernel for $\xi(r)$, which scales as $(kr)^{-1}$. Thus ω_ℓ probes a narrow range of scales in Fourier space and is insensitive to fluctuations on large scales or poorly measured or modeled small-scale structure. One can choose the range of k to be sampled by appropriate choice of r_s: more information from high k modes can be included by using smaller r_s.

As an example, the linear theory monopole statistic $\omega_0(r_s)$ is plotted in Figure 2. Plotting $r_s^2 \omega_0$ versus r_s

[6] For example, we could make the k-weight for $\ell = 0$ and $\ell = 2$ equal.

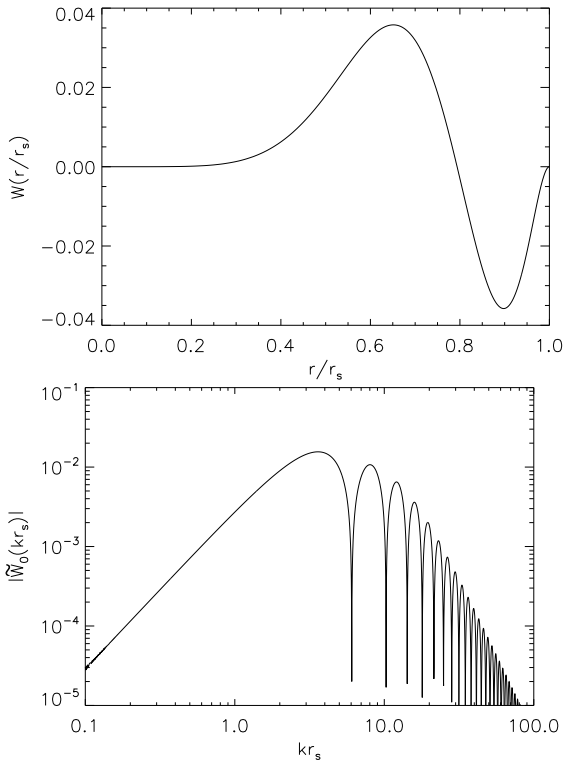

FIG. 1.— (top) The filter $W_\ell(r/r_s)$ in configuration space. There is a broad hump matching the width of the acoustic peak in $\xi(r)$ which peaks at $r \simeq 0.65\, r_s$ and a sharp (negative) spike at $0.9\, r_s$ with a width on the order of 10%. A filter of this shape will smear a feature, such as the acoustic peak in $\xi(r)$, by only a small amount which means that the acoustic information will be well localized in $\omega_\ell(r_s)$. Its compensated nature implies that $\omega_\ell(r_s)$ is not sensitive to the integral constraint. (bottom) The filter $\widetilde{W}_\ell(kr_s)$ for $\ell = 0$. The insensitivity of this filter to large scales is reflected in the fact that it is singly compensated and $\widetilde{W}_\ell \sim k^2$ as $k \to 0$. At small scales $\widetilde{W}_\ell(kr_s) \to \cos(kr_s)/(kr_s)^4$. This is a much more rapid drop-off than observed in the kernel for $\xi(r)$, which scales as $(kr)^{-1}$. These properties of the filter imply that $\omega_\ell(r_s)$ only probes a narrow range of scales in Fourier space, and that it is insensitive to large scale fluctuations or poorly constrained small-scale structure.

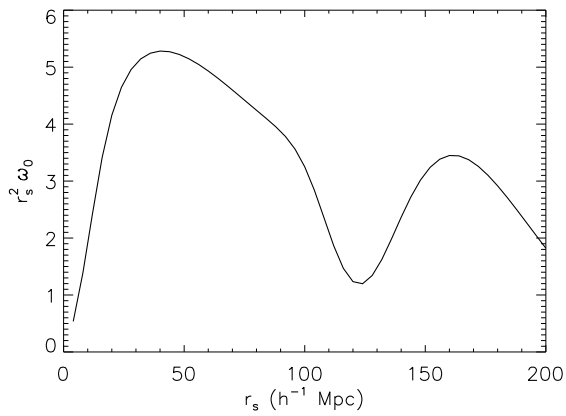

FIG. 2.— Linear theory monopole statistic $\omega_0(r_s)$. The acoustic information can be seen at the acoustic scale localized into a single dip feature.

gives a convenient vertical range. The acoustic information is mostly localized into a single dip at the acoustic scale (see §4.2.1).

2.2. *Computation*

It is possible to adapt $\omega_\ell(r_s)$ into a sum over unbinned pair counts for any sample of mass tracers following the methods described in Padmanabhan et al. (2007); there is no need to first compute $\xi(r,\mu)$. Pair counting allows us to record the redshift-space LOS and transverse distributions in an unbiased manner. Hence, like $\xi(r)$, $\omega_\ell(r_s)$ is sensitive to any anisotropies of the tracer distribution in clusters (discussed in §1).

The redshift-space correlation function can be estimated as

$$\xi_s(r,\mu) = \frac{DD(r,\mu)}{RR(r,\mu)} - 1, \tag{9}$$

where $DD(r,\mu)$ is the number of data tracer pairs separated by r and μ, while $RR(r,\mu)$ is the analogue for randomly distributed points. When analyzing observational data, the number of random points needs to be much larger than the number of data points to keep the shot-noise in RR smaller than that in DD, especially at small r. Therefore, in this case, it is important to normalize the random counts to the data counts by multiplying the RR piece by a factor of N_D^2/N_R^2, where N_D and N_R are the total number of data and random points respectively. For simulation data, however, it is not necessary to use a very large number of random points to compute RR smoothly at small scales (elicited below).

Equation (9) implies that Equation (4) can be rewritten as

$$\omega_\ell(r_s) = i^\ell \int d^3r W_\ell(r) L_\ell(\mu) \frac{DD(r,\mu)}{RR(r,\mu)}. \tag{10}$$

The -1 integrates to 0 due to the compensated nature of the filter. The RR piece is purely geometrical and is dependent only on the survey geometry (encoded in the selection function $\Phi(r,\mu)$) and the number of random points. Hence we can write RR as

$$RR(r,\mu) = n_R N_R V \Phi(r,\mu) dr d\mu \tag{11}$$

where V is the volume of a simulation or survey and n_R is the number density of random points. Normalization by N_D^2/N_R^2 as described above then takes $n_R N_R V$ to $n_D N_D V$ which is easily calculable for surveys with well defined boundaries. For observations, $\Phi(r,\mu)$ can be computed via binning methods and then fit using a smooth function $\hat{\Phi}(r,\mu)$. In the case of simulations in a periodic box, $\hat{\Phi}(r,\mu) = 1$ as all tracer particles are "detected" with the same probability by construction. With these points in mind, we can now pick arbitrarily small bins when computing the DD piece since RR has been approximated by a smooth function and hence does not suffer from shot-noise induced through pair-counting. As is such, we may employ a binning scheme in which there is either zero or one DD pair per bin. This step reduces the integral in Equation (10) to a sum over DD pairs as in

$$\omega_\ell(r_s) = i^\ell \sum_{i \in DD} \frac{W_\ell(r_i) L(\mu_i)}{n_D N_D V \hat{\Phi}(r_i,\mu_i)}. \tag{12}$$

2.3. *Covariance Matrix*

Since ω_ℓ is an unbinned quantity, we can in principle estimate it at as many r_s values as we wish without affecting the signal in the adjacent values – there is no bin which is made smaller. However adjacent points become increasingly correlated as the r_s spacing decreases, compromising the usefulness of very fine sampling.

In the Gaussian limit, the covariance matrix is

$$\mathrm{Cov}\left[\omega_\ell(r_s), \omega_{\ell'}(r_s')\right] = \frac{2(2\ell+1)(2\ell'+1)}{V} \times \int \frac{k^2 dk}{2\pi^2} \widetilde{W}_\ell(kr_s) \widetilde{W}_{\ell'}(kr_s') \mathcal{I}_{\ell\ell'}(k) \tag{13}$$

with

$$\mathcal{I}_{\ell\ell'} = \frac{1}{2} \int d\mu L_\ell(\mu) L_{\ell'}(\mu) \left[\sum_L P_L(k) L_L(\mu) + \aleph \right]^2 \tag{14}$$

where $\sum P_L(k) L_L(\mu)$ is the legendre decomposition of the full 3D power spectrum $P(\vec{k})$ and $\aleph$ is shot-noise. Assuming Poisson shot-noise, $\aleph = \bar{n}^{-1}$, where $\bar{n}$ is the number density of the mass tracer.

2.4. *Summary of Key Features*

We conclude this section with a summary of the key features and advantages of $\omega_\ell(r_s)$ over $\xi(r)$ and $P(k)$ estimators.

1. $\omega_\ell(r_s)$ has a compensated filter that reduces sensitivity to poorly constrained large scale power and circumvents the integral constraint. $\xi(r)$, on the other hand, experiences these problems. The compensated filter also makes $\omega_\ell(r_s)$ measured in different subvolumes of the survey more independent which is important for attaining robust error estimates from methods such as bootstrap and jackknife.

2. The filter is approximately compact in both configuration and Fourier space. The smoothness in configuration space leads to the steep drop-off at high k in Fourier space. This effectively minimizes the impact of large k or small scale power which is not well constrained in large cosmological surveys. The filter is localized in configuration space which means that, unlike in $P(k)$, the acoustic information is localized in $\omega_\ell(r_s)$. However, it is not as localized as in $\xi(r)$ (see §4.2.1).

3. Like $\xi(r)$, $\omega_\ell(r_s)$ can be easily adapted into a pair count statistic, so the distribution of tracers in both the LOS and transverse directions can be recorded accurately. Hence, it is unbiased and sensitive to any anisotropies in the clustering of tracers. These can be used to determine the underlying cosmology. $P(k)$ estimators do not typically allow this type of analysis.

4. $\omega_\ell(r_s)$ is an unbinned statistic, unlike $\xi(r)$ and $P(k)$.

While the setbacks of traditional $P(k)$ and $\xi(r)$ estimators are minor, it is beneficial to have a statistic like $\omega_\ell(r_s)$ which combines many of the advantages of both.

3. SIMULATIONS AND ANALYSIS METHODS

A major goal in developing this new statistic is to use it for better measuring and calibrating the acoustic scale. The monopole statistic $\omega_0(r_s)$ is especially useful in this regard as it is a direct map from the traditional 2-point correlation function and power spectrum. In this section, we implement $\omega_0(r_s)$ and demonstrate how it can be used to measure the shift in the acoustic peak.

3.1. *Simulations*

We use an innovative N-body code named ABACUS (Metchnik & Pinto 2010) to simulate the evolution of large scale structure from an initial density field. This code can achieve very high force accuracy with relatively small computational effort as it does away with the tedious Fourier methods traditionally used to treat periodic boundary conditions. Instead, Metchnik & Pinto (2010) show the equivalence of Ewald summation and infinite direct summation with the addition of one extra term, and subsequently derive and exploit the computational advantages of the latter. In particular, it is possible to expand the far-field contribution to the direct force summation into multipoles. The multipole moments are the same in every periodic box and hence can be factored out of the sum. The derivative terms remaining inside the sum depend only on how each cell is partitioned and hence need only be computed once. Expansion into multipoles also allows one to compute the force summation to arbitrary accuracy. It is therefore possible to achieve high computational efficiency and accuracy with comparatively short run-times.

We derive our results in redshift-space at $z = 1$ from a set of 44 simulations with 1024^3 dark matter particles in each. The simulations were performed in $1h^{-1}$ Gpc periodic boxes with the WMAP5+SN+BAO best-fit cosmological parameters: $\Omega_m = 0.279$, $\Omega_\Lambda = 0.721$, $h = 0.701$, $\Omega_b = 0.0462$, $n_s = 0.96$ and $\sigma_8 = 0.817$ (Komatsu et al. 2009) which implies a particle mass of $7.2 \times 10^{10} h^{-1} M_\odot$. The initial conditions are generated via the second-order Lagrangian perturbation theory code of Sirko (2005) at $z = 50$ with no extra power for the box scale.

3.2. *Halo Occupation Distributions*

We use a simple friends-of-friends (Davis et al. 1985) method with a linking length equal to 0.16 of the interparticle spacing to identify the collapsed dark matter halos in our simulations. We then populate these halos with galaxies by applying simple HODs based on the form

$$\langle N_g(M)\rangle = [1 + (M/M_{\rm sat})^\gamma]\exp(-M_{\rm cen}/M) \qquad (15)$$

where M is the halo mass, $M_{\rm cen}$ is the minimum mass for a halo to contain a central galaxy, $M_{\rm sat}$ is the minimum mass for a halo to contain at least one satellite, and γ is an exponential parameter that we set to 1 (Guzik & Seljak 2002; Berlind et al. 2003; Kravtsov et al. 2004; Zheng et al. 2005). We assign a central galaxy to a halo if $M > M_{\rm cen}$, this is a good approximation to $\langle N_{\rm cen}(M)\rangle = \exp(-M_{\rm cen}/M)$. The central galaxy is taken to be at the halo's center of mass and assigned the center of mass velocity. If a halo is assigned a central galaxy, then the number of satellite galaxies is determined by generation of a random integer based on a Poisson distribution with mean equal to $\langle N_{\rm sat}(M)\rangle = (M/M_{\rm sat})^\gamma$. We then randomly pick a corresponding number of halo particles and assign their positions and velocities to the satellites.

In order to compare the peak shifts derived using $\omega_0(r_s)$ and $P(k)$ in a range of models, we apply three different HODs to our simulations. The properties of these HODs are described in Table 1 and obtained by adjusting the values of $M_{\rm cen}$ and $M_{\rm sat}$. We also list the properties of a dark matter (DM) only case that is merely a 0.4% subsample of the particles in each simulation. We compute $\omega_0(r_s)$ in redshift-space via the pair counting method detailed in §2.2 within the range $5h^{-1}$ Mpc $\leq r_s \leq 200h^{-1}$ Mpc using $5h^{-1}$ Mpc spacing. We also compute σ_8 using a similar pair counting method derived from the configuration space equation

$$\sigma_R^2 = \int_0^{2R} \frac{1}{R^3}\left(3 - \frac{9}{4}\frac{r}{R} + \frac{3}{16}\left(\frac{r}{R}\right)^3\right) r^2\xi(r)dr. \qquad (16)$$

3.3. *Fitting $\omega_0(r_s)$ to Measure the Peak Shift*

We fit the redshift-space $\omega_0(r_s)$ using the form

$$P_{\rm sim}(k) = B(k)P_m(k/\alpha) + A(k) \qquad (17)$$

where

$$B(k) = \frac{(b_1^2 + b_2^2 k + b_3^2 k^2)}{1 + r_{\rm scale}k} \qquad (18)$$

and $A(k)$ transforms into $A(r_s) = a_1 r_s^{-9}$ in r_s space. Such a form for $A(k)$ is motivated by the fact that we want to marginalize over the shape of the correlation function at small scales (i.e., the contribution of the 1-halo term). Expanding Equation (8), we see that $W(x) = (-4x^5 + 2x^4 - 8x^3 + 2x^2)\frac{1}{r_s^3}$. This implies that the highest order term in r_s is r_s^{-9}. At small scales, this is the term that will dominate in the transformation from $\xi(r)$ to $\omega_0(r_s)$ as defined by Equation (4).

$P_m(k)$ is the template power spectrum we use for our fitting. To account for the degradation of the acoustic peak through nonlinear evolution and redshift distortions, the template model $P_m(k)$ is obtained from the linear power spectrum $P_{\rm lin}(k)$ at $z = 1$ by the modification

$$P_m(k) = [P_{\rm lin}(k) - P_{\rm smooth}(k)]\exp(-k^2\Sigma_{\rm nl}^2/2) + P_{\rm smooth}(k) \qquad (19)$$

where $P_{\rm smooth}$ is the dewiggled power spectrum described in Eisenstein & Hu (1998) and $\Sigma_{\rm nl}$ is a nonlinear parameter used to degrade the peak (Eisenstein et al. 2005; Tegmark et al. 2006; Crocce & Scoccimarro 2006; Eisenstein et al. 2007; Crocce & Scoccimarro 2008; Matsubara 2008). To allow maximum flexibility in our marginalization, we fit over $\Sigma_{\rm nl}$ and the other nonlinear nuisance parameter in equation (17), $r_{\rm scale}$.

Our scale dilation parameter α represents the shift in the acoustic peak. Under this formalism, $\alpha > 1$ indicates a shift towards smaller scales and $\alpha < 1$ indicates a shift towards larger scales. Physically, α is the ratio between the linear theory acoustic scale (150 Mpc) to the measured acoustic scale. Since all the terms in the fitting function are additive, the basis functions $P_m(k/\alpha)/(1 + r_{\rm scale}k)$, $kP_m(k/\alpha)/(1 + r_{\rm scale}k)$,

$k^2 P_m(k/\alpha)/(1 + r_{\rm scale}k)$ and r_s^{-9} for a fixed α, $\Sigma_{\rm nl}$ and $r_{\rm scale}$ can be easily mapped into r_s space (if necessary) using equation (6) where upon a least-squares fit can be performed against $\omega_0(r_s)$ from the simulations to obtain values for the linear nuisance parameters b_1, b_2, b_3 and a_1. As we are interested in the acoustic feature, we use a fitting range of $30 \leq r_s \leq 200h^{-1}$ Mpc. For an r_s spacing of $5h^{-1}$ Mpc, this implies 27 degrees of freedom in the fit.

We assume that the errors on $\omega_0(r_s)$ can be well approximated by the covariance matrix C assuming Poisson shot-noise (see §3.4) with the addition of nonlinear shot-noise. We also assume that the monopole ($\ell = 0$) dominates $P(\vec{k})$ so that all higher order contributions to the power spectrum are effectively zero. This amounts to computing C using $P(\vec{k}) = P_m(k)$ as the input power spectrum, where we take a fixed $\Sigma_{\rm nl} = 7.0h^{-1}$ Mpc at $z = 1$ in redshift-space following Seo et al. (2008). We normalize this power spectrum to the amplitude of the redshift-space power spectrum through multiplication by the bias squared defined as $b^2 = (\sigma_{8,\rm case}/\sigma_{8,\rm matter})^2$. $\sigma_{8,\rm case}$ values are given in Table 2 and $\sigma_{8,\rm matter} = 0.506$ in real space at $z = 1$ in linear theory. We then iteratively scale by b_1^2 obtained through fitting until the output b_1^2 is close to 1. This iterative normalization scheme is to make the input power spectrum as close as possible to the form being fit so that the computed covariance matrix is a reliable estimate of the errors.

The shot-noise we enter into the calculation of C includes a nonlinear component (quoted in Table 1) in addition to the Poisson shot-noise $\bar{n}^{-1}$ as described in Equation (13). This additional shot-noise is a result of nonlinear structure formation on small scales. We estimate this nonlinear shot-noise as

$$\aleph_{\rm nonlin} = \int_0^{r_{\rm nonlin}} 4\pi r^2 [\xi(r) - \xi_{\rm lin}(r)] dr \qquad (20)$$

where $\xi(r)$ is the correlation function averaged over the 44 simulations for each HOD, $\xi_{\rm lin}(r)$ is the linear correlation function at $z = 1$ and $r_{\rm nonlin}$ is the scale above which nonlinear effects become unimportant. We take $r_{\rm nonlin}$ to be $10h^{-1}$ Mpc. The resulting $\aleph_{\rm nonlin}$ is a rough estimate of the excess small scale correlation due to nonlinear evolution. Since it makes little difference whether all of this extra shot-noise comes in at zero separation in r or through the extended effects of the one-halo term, which is only important at small r, we assume the excess correlation to be a spike at $r = 0$ for convenience. When transformed into k space, this gives a constant and becomes extra white noise that we add on to every mode equally, in addition to the Poisson shot-noise. For the subsampled DM case, the linear and the measured correlation functions were sufficiently similar at 1-10h^{-1} Mpc to warrant taking $\aleph_{\rm nonlin} = 0$ for this case. Alternatively, one can also account for nonlinear shot-noise by computing the covariance matrix using the nonlinear power spectrum.

The χ^2 likelihood indicator corresponding to the best-fit linear nuisance parameters for fixed α, $\Sigma_{\rm nl}$ and $r_{\rm scale}$ is then

$$\chi^2 = (\vec{\omega}_0 - \vec{m})^T C^{-1} (\vec{\omega}_0 - \vec{m}) \qquad (21)$$

where $\vec{\omega}_0$ is $\omega_0(r_s)$ measured from the simulations, $\vec{m}$ is the best-fit model and C^{-1} is the inverse of the covariance matrix. We compute the best-fit values of α, $\Sigma_{\rm nl}$ and $r_{\rm scale}$ by minimizing χ^2 of the fits for the DM case and for each HOD using a generalized reduced gradient method from IDL. We quote the bias for each case as $\sigma_{8,\rm case}/\sigma_{8,\rm matter}$ multiplied by the additional scaling factors of b_1 described above.

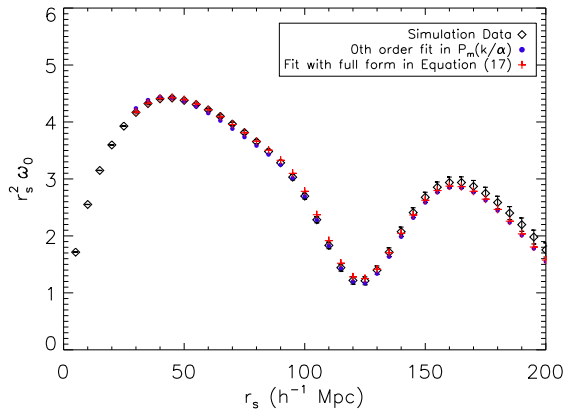

FIG. 3.— $\omega_0(r_s)$ averaged over all 44 simulations for HOD1 (black diamonds). Overplotted are a fit obtained through the form in Equation (17) (red crosses) and a $0th$ order fit in $P_m(k/\alpha)$ (purple dots), both over a range of $30 \leq r_s \leq 200h^{-1}$ Mpc. One can see that the $0th$ order fit already appears quite good with $\chi^2 = 2.26$ per dof. However, by introducing additional nuisance parameters, the quality of the fit over the specified range improves further to $\chi^2 = 0.97$ per dof.

We plot $\omega_0(r_s)$ averaged over all 44 simulations for HOD1 in Figure 3. The fit obtained through the form in Equation (17) and a $0th$ order fit obtained by just a rescaling of $P_m(k/\alpha)$ are overplotted. Although the $0th$ order fit already appears quite good, one can see that introducing additional nuisance parameters improves the quality of the fit even more over the fitting range. The χ^2 per degree of freedom (dof) improves from 2.26 to 0.97.

Using this fitting technique, we derive values of bias, α and associated errors for each of our three HODs and our DM case via the resampling methods described in the following section.

3.4. *Resampling Methods*

We use two different methods to measure the mean peak shift α and the scatter in the mean σ_α for each case in Table 1. The first is a modified jackknife technique in which we randomly select M out of N simulations at a time without replacement, average their $\omega_0(r_s)$ and fit this average. We repeat this 1000 times and extract a mean b_1 for computing the bias, an average α and a scatter in α. This scatter needs to be rescaled by an additional factor of $f = \sqrt{M}/\sqrt{N - M}$ in order to reflect the scatter asscociated with the mean of α for N simulations. For our simulations we have $N = 44$ and take $M = 22$. With this choice of M, $f = 1$ and so the scatter in α reflects the error in the mean of α. This method is useful in that it provides us with a large set of α's from which we can easily derive a mean α and σ_α.

The fit results for the subsampled DM case as well as for each HOD model are quoted in Table 2. The average values of $\Sigma_{\rm nl}$ and r_{scale} are also included for completeness, however the focus of this paper is on α. The somewhat low value of χ^2 per dof for HOD3 suggests that we

are overestimating the amount of nonlinear shot-noise. We are also approaching the shot-noise limited regime for HOD3 as evidenced by the fact $\bar{n}P_{0.2} \approx 1.6$. We note here that we used χ^2 only to find the best-fit α for each HOD, not to generate the errors. Hence, the fact that our reduced χ^2 values are slightly deviant from unity does not hinder the error estimation.

The second method we use is jackknife resampling. The results obtained using this method are in good agreement with the first method. This indicates that the error estimates obtained using our first method are robust in comparison to more traditional methods.

By using these resampling techniques, any non-Gaussian effects not accounted for by assuming a Gaussian covariance matrix while fitting (as in §3.3) will be reflected in σ_α.

4. COMPARISON TO THE POWER SPECTRUM

4.1. *Comparison from Simulations*

An important step in implementing this new statistic is to show that it produces consistent results when compared to established methods and can therefore be an effective calibrator of the acoustic scale. We do this by comparing the peak shifts measured from the same set of simulations via the new $\omega_0(r_s)$ statistic and the traditional $P(k)$ method (see Seo et al. (submitted) and Mehta et al. (in prep) for details).

As we use the same 1000 random sets of M simulations as Seo et al. (submitted) and Mehta et al. (in prep), there should be a 1:1 correspondance between the α's derived from $\omega_0(r_s)$ and $P(k)$ for the DM case and for each HOD. It should be noted that Seo et al. (submitted) and Mehta et al. (in prep) use different $P(k)$ fitting forms from the one detailed in §3.3. They employ two fitting forms, both of which can also be described by equation (17). The first form has $B(k)$ as a $2^{\rm nd}$ order polynomial and $A(k)$ as a $7^{\rm th}$ order polynomial. The second form uses Pade approximants for $B(k)$, i.e., $B(k) = b_0(1+c_1k+c_3k^2+c_5k^3)/(1+c_2k+c_4k^2)$ and a $2^{\rm nd}$ order polynomial for $A(k)$. In this paper, we will compare the α's measured from $\omega_0(r_s)$ against those measured from $P(k)$ by Seo et al. (submitted) (DM) and Mehta et al. (in prep) (HODs) using the first form. It should also be noted here that the $P(k)$ results obtained for the DM case by Seo et al. (submitted) utilize the full DM sample whereas we have subsampled to reduce computation time in this work.

Figure 4 shows α from $\omega_0(r_s)$ versus α from $P(k)$ for the 1000 fit iterations performed on HOD2 (top) and DM (bottom). The red cross indicates the mean α values with their associated errors. The central grey line is a line with slope unity that passes through the mean. The two outer grey lines indicate the 1σ boundaries associated with $\Delta\alpha_{\omega P}$. These indicate that the correlation is 1σ consistent with a line of slope unity that has a y-intercept of 0 for both HOD2 and the DM case implying that the two α sets are consistent with each other. The same holds for HOD1 but HOD3 is slightly more deviant with 1.6σ agreement between $\omega_0(r_s)$ and $P(k)$. The larger discrepancy between the HOD3 results may be due to the fact that shot-noise is becoming significant in this case (as shown in §3.4). It could also be that shot-noise affects $P(k)$ and $\omega_0(r_s)$ differently or the nuisance parameters

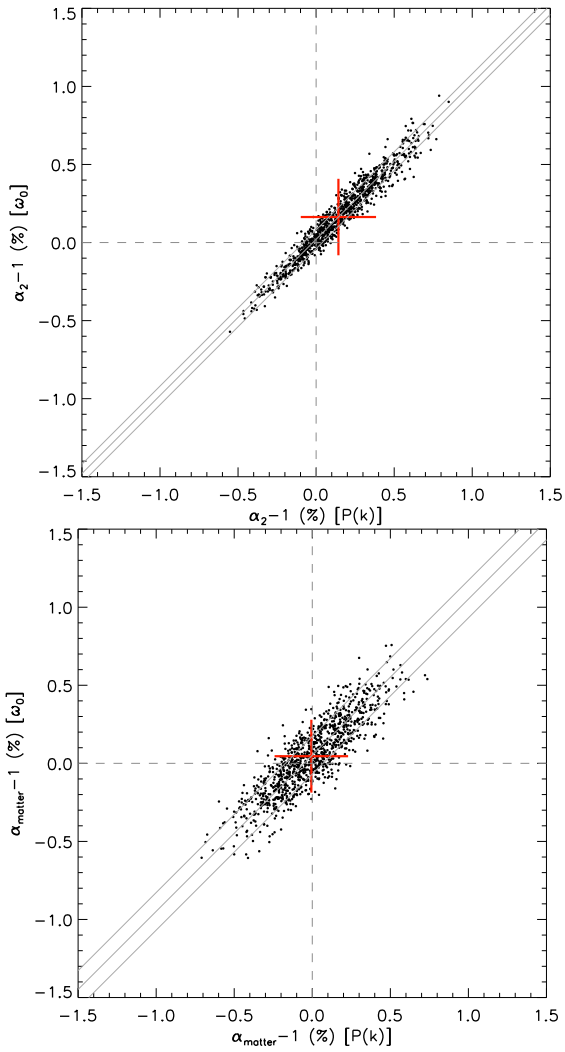

FIG. 4.— α from $\omega_0(r_s)$ versus α from $P(k)$ for HOD2 (top) and DM (bottom). The data points are from a resampling technique in which we randomly pick $M = 22$ simulations out of $N = 44$ total and fit the averaged $\omega_0(r_s)$ from these M simulations. We repeat this 1000 times and hence obtain 1000 values of α. The scatter on α needs to be rescaled by $\sqrt{M}/\sqrt{N-M}$ to reflect the true scatter on the mean. For our choice of M, this scaling factor is equal to 1. Hence the scatter in the plot truly reflects the scatter on the mean of α. The red cross marks the mean α values with their associated errors. The central grey line has unity slope and passes through the mean. The two outer grey lines delineate the 1σ boundaries associated with $\Delta\alpha_{\omega P}$. As the data points lie largely in between the 1σ lines with a slope similar to unity for both HOD2 and the DM case (see Table 3), we conclude that the two α sets are consistent with each other. The same correlation is observed for HOD1. HOD3 shows 1.6σ agreement between $\omega_0(r_s)$ and $P(k)$. This slightly larger discrepancy may be due to the fact that shot-noise is becoming significant in this low number density case. Also, shot-noise may affect $P(k)$ and $\omega_0(r_s)$ differently or the nuisance parameters may not be fully handling the scale-dependence of a high-bias HOD such as HOD3. The large scatter in the DM case is likely due to the subsampling of matter in the computation of $\omega_0(r_s)$ but not in $P(k)$. The overall agreement between the $\omega_0(r_s)$ and $P(k)$ results imply that distance measures will be consistent between the two.

are not fully handling the scale-dependence of a high-bias HOD such as HOD3. The large scatter in the DM case is likely due to the fact that we have subsampled the matter in our computation of $\omega_0(r_s)$ but not in $P(k)$. The mean differences, $\Delta\alpha_{\omega P} = \langle\alpha_\omega - \alpha_P\rangle$, for the DM case as well

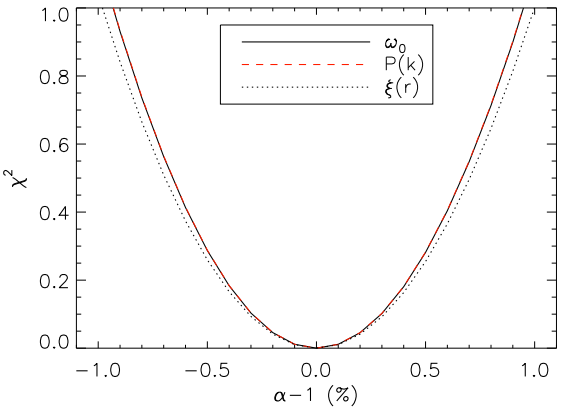

FIG. 5.— χ^2 versus α for fits in $\omega_0(r_s)$, $P(k)$ and $\xi(r)$. We shift the acoustic feature from linear theory by a given α (here $\alpha_{given} = 1.0$) and run our fit algorithms to see how well we can recover this input. For $\omega_0(r_s)$ we fit between $r_s = 50\text{-}200h^{-1}$ Mpc, for $P(k)$ we fit between $k = 0.0\text{-}1.2h$ Mpc^{-1} and for $\xi(r)$ we fit between $r = 50\text{-}200h^{-1}$ Mpc. The parabolic shape of the curves is due to the fact that $\omega_0(r_s)$, $P(k)$ and $\xi(r)$ are derived from a Gaussian random field in linear theory. The width of the parabola at $\chi^2 = 1$ is then the theoretical σ_α of the fit. The $\omega_0(r_s)$ and $P(k)$ curves overlap nicely, implying that the σ_α ratio between $\omega_0(r_s)$ and $P(k)$ is ~ 1. This indicates that for the given fitting ranges $\omega_0(r_s)$ and $P(k)$ contain equal amounts of acoustic information. Hence, the same amount of acoustic information can be obtained through either $\omega_0(r_s)$ or $P(k)$ from analysis of equal volume surveys.

as for each HOD are given in Table 3 along with their 1σ errors. One can see that the α's from most of the cases are 1σ consistent between $\omega_0(r_s)$ and $P(k)$, indicating that distance measures will be consistent between the two statistics. Hence we conclude that $\omega_0(r_s)$ is a well-tuned statistic for analysis of BAOs.

4.2. *Theory Constraints on σ_α*

As we wish to promote $\omega_0(r_s)$ as an alternative method for analyzing the BAO, it is necessary to show how much acoustic information can be extracted from $\omega_0(r_s)$ relative to $P(k)$ and $\xi(r)$ for surveys of the same size. We do this by shifting the acoustic feature in the linear theory $\omega_0(r_s)$, $P(k)$ and $\xi(r)$ by a given α and then running our fit algorithms to see how well we can recover this input α. For $\omega_0(r_s)$ we fit between $r_s = 50\text{-}200h^{-1}$ Mpc in r_s spacings of $2.5h^{-1}$ Mpc; for $P(k)$ we fit between $k = 0.0\text{-}1.2h$ Mpc^{-1} in $\log(k)$ spacings of ~ 0.002; and for $\xi(r)$ we fit between $r = 50\text{-}200h^{-1}$ Mpc in r spacings of $1h^{-1}$ Mpc. We use the same fitting technique as described in §3.3 but with different forms for $B(k)$ and $A(k)$ that are then transformed to r and r_s space to fit $\omega_\ell(r_s)$ and $\xi(r)$ respectively. We pick $B(k) = b$, where b is the large-scale bias, and $A(k)$ to be the cold dark matter-only power spectrum multiplied by a set of cubic spline functions specified at $k = 0.0\text{-}1.08h$ Mpc^{-1} in spacings of $dk = 0.12h$ Mpc^{-1} and the derivative specified at the first spline point. The spline functions are taken to be natural (i.e., second derivative equal to 0) at the last spline point, beyond which a linear extrapolation is implemented. This choice of $A(k)$ ensures convergence when transformed to r_s space and makes the fits in $P(k)$, $\xi(r)$ and $\omega_0(r_s)$ readily comparable. We assume a survey volume of $1h^{-1}$ Gpc with $\aleph = 1000$ (i.e., one million particles). As a cross check, we confirmed that this new fitting form does in fact give similar results to the form used in §3.3.

Figure 5 plots the χ^2 versus α for $\omega_0(r_s)$, $P(k)$ and $\xi(r)$. Here the input α is equal to 1. If $\omega_0(r_s)$, $P(k)$ and $\xi(r)$ are derived from a Gaussian random field as they are in linear theory, we would expect that χ^2 versus α be parabolic as shown in the figure. The width of the parabola at $\chi^2 = 1$ is then the theoretical σ_α from the fit. The overlap between the $\omega_0(r_s)$ and $P(k)$ curves indicates that the ratio of σ_α for $\omega_0(r_s)$ to $P(k)$ is ~ 1. This means that for the given fitting ranges $\omega_0(r_s)$ and $P(k)$ contain equal amounts of acoustic information. Since, volume is proportional to χ^2 which is proprotional to σ^{-2}, an important implication is that we are able to obtain the same amount of acoustic information using either $\omega_0(r_s)$ or $P(k)$ from analysis of equal volume surveys. We emphasize here that the results presented in this section assume idealized linear theory forms for $P(k)$, $\xi(r)$ and $\omega_0(r_s)$. In practice, numerous physical and observational effects distort the measured statistics from these ideals. However, we expect that the features described in §2 will reduce the impact of troublesome observational effects in any BAO analysis using $\omega_0(r_s)$.

4.2.1. *Locating the Acoustic Information*

It is useful to track down where the acoustic information lies and how it changes with α in $\omega_0(r_s)$, $\xi(r)$ and $P(k)$. This is reflected in the derivatives $d\omega_0/d\alpha$, $d\xi/d\alpha$ and $dP/d\alpha$ after marginalizing out the broadband shape. To do this, we calculate the residuals from the $P(k)$ fits described in §4.2 for $\alpha = 0.996$ and $\alpha = 1.004$. We then take $dP/d\alpha$ as the difference between these residuals divided by $1.004 - 0.996 = 0.008$. The transformations of $dP/d\alpha$ into r_s and r space then give us $d\omega_0/d\alpha$ and $d\xi/d\alpha$ respectively. We have plotted $dP/d\alpha$ in the top panel of Figure 6, $d\xi/d\alpha$ in the middle panel and $d\omega_0/d\alpha$ in the bottom panel. It is evident from these plots that the acoustic information is not as localized in $\omega_0(r_s)$ as in $\xi(r)$, but it is still reasonably well localized. The bottom panel of Figure 6 indicates that the optimal fitting range that will include all of the acoustic information encoded in $\omega_0(r_s)$ is somewhere within the range $r_s = 30\text{-}300h^{-1}$ Mpc.

The top panel of Figure 7 shows how σ_α changes as the minimum r_s of the fitting range is stepped up from $30\text{-}90h^{-1}$ Mpc with the maximum r_s of the fitting range fixed at $300h^{-1}$ Mpc. The bottom panel of Figure 7 shows how σ_α changes as the maximum r_s of the fitting range is stepped down from $300\text{-}110h^{-1}$ Mpc with the minimum r_s of the fitting range fixed at $30h^{-1}$ Mpc. One can see that when the minimum of the fitting range is larger than $50h^{-1}$ Mpc, σ_α begins to deviate, indicative of missing some of the acoustic information. This also happens when the maximum of the fitting range is smaller than $140h^{-1}$ Mpc. Hence, the minimum fitting range that allows one to extract all of the acoustic information appears to be $r_s = 50\text{-}140h^{-1}$ Mpc. We caution, however, against using this fitting range for analysis because Figure 6 indicates that there is acoustic information beyond $140h^{-1}$ Mpc in r_s space. Our specific choice of filter is forcing $\omega_0(r_s)$ to be smooth which may be why, once we have sampled over the peak at $\sim 130h^{-1}$ Mpc, we can predict the shape of the curve accurately without

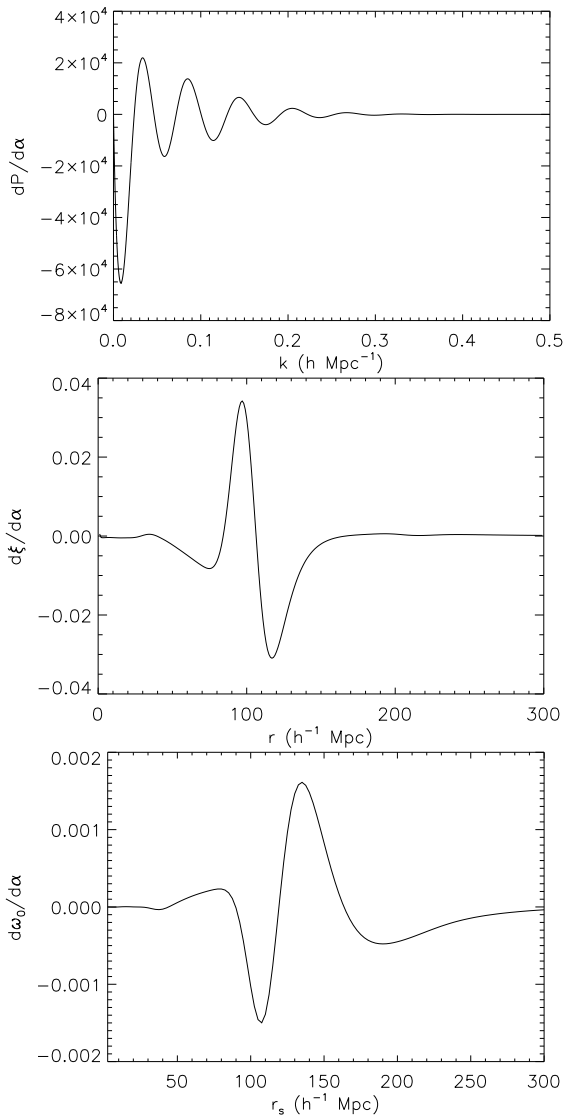

FIG. 6.— (top) $dP/d\alpha$ calculated from the residuals of the $P(k)$ fits after marginalizing out the broadband shape. The change in $P(k)$ with α captured by $dP/d\alpha$ should correspond to how the acoustic information is shifted as α changes. (middle) $d\xi/d\alpha$ obtained by transforming $dP/d\alpha$. This shows where the acoustic information is located in configuration space and how it changes with α. (bottom) $d\omega_0/d\alpha$ obtained by transforming $dP/d\alpha$ to r_s space. This shows where the acoustic information is located in r_s space and how it changes with α. Comparison with the middle panel indicates that the acoustic information is not as localized in $\omega_0(r_s)$ as it is in $\xi(r)$, however, it is still reasonably well localized. All of the acoustic information is located within $r_s \sim$ 30-300h^{-1} Mpc, indicating that the optimal fitting range for $\omega_0(r_s)$ is somewhere within these limits.

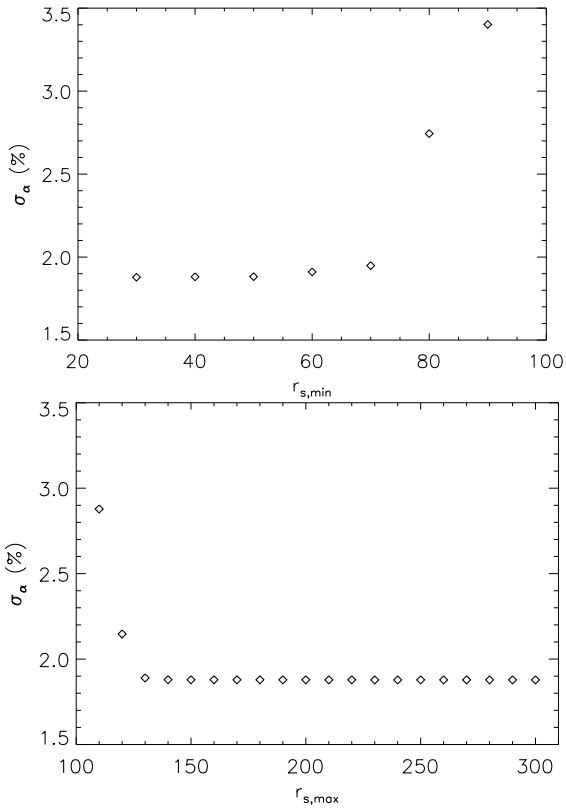

FIG. 7.— (top) Plots how σ_α changes as the minimum r_s of the fitting range is stepped up from 30-90h^{-1} Mpc with the maximum r_s of the fitting range fixed at 300h^{-1} Mpc. The deviation of σ_α at $r_{s,min}$ larger than 50h^{-1} Mpc indicates that some of the acoustic information is being missed by this fitting range. (bottom) Plots how σ_α changes as the maximum r_s of the fitting range is stepped down from 300-110h^{-1} Mpc with the minimum r_s of the fitting range fixed at 30h^{-1} Mpc. The deviation of σ_α at $r_{s,max}$ smaller than 140h^{-1} Mpc indicates that some of the acoustic information is being missed by this fitting range. The above analysis implies that in order to extract all of the acoustic information, one should fit between $r_s =$ 50-140h^{-1} Mpc. However, Figure 6 indicates that there is acoustic information beyond 140h^{-h} Mpc in r_s space, so we caution against using this fitting range for analysis. It is possible that our specific choice of filter is forcing $\omega_0(r_s)$ to be smooth, so once we have sampled over the peak at $\sim$ 130h^{-1} Mpc, the shape of the curve can be predicted accurately without fitting to larger r_s. We recommend extending the maximum of the fitting range out to around 200h^{-1} Mpc, at the expense of computation time, to ensure a robust measurement of the acoustic information.

fitting to larger r_s (i.e., there is very little χ^2 contribution from large scales). Although it would increase the computation time, we recommend extending the maximum of the fitting range out to around 200h^{-1} Mpc to ensure a robust measurement of the acoustic information. This is the motivation behind picking the fitting range for $\omega_0(r_s)$ to be $r_s =$ 50-200h^{-1} Mpc in Figure 5.

5. CONCLUSIONS

We have presented a new statistic $\omega_\ell(r_s)$ for analyzing baryon acoustic oscillations. This new statistic is advantageous over the traditional methods used to estimate $\xi(r)$ and $P(k)$ as it does away with many of their setbacks. Estimators of $\xi(r)$ are sensitive to poorly measured large scale power through effects such as the integral constraint, whereas the compensated nature of the filter $W_\ell(r)$ used to compute $\omega_\ell(r_s)$ circumvents this problem. This feature of the filter also makes $\omega_\ell(r_s)$ measured in different subvolumes of a survey more independent which makes error estimation methods such as bootstrap and jackknife more robust. Estimators of $P(k)$ give the true density field convolved with a window function making the measured statistic biased. Attempting to deconvolve the window function introduces artificial smoothing at small separations in k due to their near delta function shapes in real observational surveys. $\omega_\ell(r_s)$, on the other hand, does not suffer from this as it is a pair count statistic. Pair counting allows us to accurately note the unbiased distribution of tracers both

along the LOS and in the transverse direction. The fact that the distribution can be recorded accurately also means that $\omega_\ell(r_s)$ is sensitive to anisotropic clustering. Hence it can also be used to probe the underlying cosmology. In addition, there is no need to worry about binning related issues when computing $\omega_\ell(r_s)$ as it is an unbinned statistic. The smoothness of the filter in configuration space causes the rapid fall-off of the filter in Fourier space. This reduces the impact of large k modes or small scales which are not well constrained in large cosmology surveys. The localized nature of $W_\ell(r)$ is conducive to minimal smearing of the acoustic information so that it is mostly concentrated in a single dip at the acoustic scale. This is simpler to analyze than the oscillatory acoustic features in $P(k)$.

We also showed that with the present form for $W_\ell(r)$ and a finite fitting range encompassing the acoustic scale, it is possible to extract the same amount of acoustic information using either $\omega_0(r_s)$ or $P(k)$ from equal volume surveys. It is important to note that these results were obtained through analysis of idealized linear theory forms for $P(k)$, $\xi(r)$ and $\omega_0(r_s)$. In practice, the measured forms of these statistics are distorted by various physical and observational effects. However, we expect that the features described in §2 will reduce the impact of troublesome observational effects in any BAO analysis using $\omega_0(r_s)$. We also demonstrated where the acoustic information is located in $\omega_0(r_s)$, $\xi(r)$ and $P(k)$ and how it changes with α. From this analysis, the minimum fitting range required to extract all of the acoustic information from $\omega_0(r_s)$ appears to be $r_s = 50\text{-}140h^{-1}$ Mpc. However, we recommend extending the maximum of the fitting range out to around $200h^{-1}$ Mpc to ensure a robust measurement of the acoustic information.

We compared the acoustic peak shifts derived using $\omega_0(r_s)$ to those derived using $P(k)$ for a pure DM case as well as for three halo based galaxy models. The results for the DM and the higher number density cases are all much better than 1σ consistent with each other. The low number density case is slightly deviant with 1.6σ agreement between $\omega_0(r_s)$ and $P(k)$. This may be a result of approaching the shot-noise limited regime or our lack of understanding of shot-noise in general and how it may affect $P(k)$ and $\omega_0(r_s)$ differently. It may also be caused by our fitting form not handling the scale-dependence of high-bias models in full. The general consistency betwen $\omega_0(r_s)$ and $P(k)$ is encouraging and implies that distance measures will be consistent between the two methods. From this and the features listed above, we conclude that $\omega_0(r_s)$ is a well-tuned new statistic for BAO analysis.

This work is supported by NASA BEFS NNX07AH11G and NSF AST-0707725.

REFERENCES

Alcock, C., & Paczynski, B. 1979, Nature, 281, 358
Amendola, L., Quercellini, C., Giallongo, E. 2005, MNRAS, 357, 429
Angulo, R., et al. 2008, MNRAS, 383, 755
Baumgart, D. J., & Fry, J. N. 1991, ApJ, 375, 25
Berlind, A. A., et al. 2003, ApJ, 593, 1
Blake, C., & Glazebrook, K. 2003, ApJ, 594, 665
Blanchard, A., & Alimini, J.-M. 1998, A&A, 203, L1
Bond, J. R., & Efstathiou, G. 1984, ApJ, 594, 665
Cole, S., Fisher, K. B., Weinberg, D. H. 1994, MNRAS, 267, 785
Cole, S., Fisher, K. B., Weinberg, D. H. 1995, MNRAS, 275, 515
Crocce, M., & Scoccimarro, R. 2006, Phys. Rev. D, 73, 063520
Crocce, M., & Scoccimarro, R. 2008, Phys. Rev. D, 77, 023533
Davis, M., & Peebles, P. J. E. 1983, ApJ, 267, 465
Davis, M., Efstathiou, G., Frenk, C. S., White, S. D. M. 1985, ApJ, 292, 371
de Lapparent, V., Geller, M. J., Huchra, J. P. 1988, ApJ, 332, 44
Eisenstein, D. J., & Hu, W. 1998, ApJ, 496, 605
Eisenstein, D. J., Hu, W., Tegmark, M. 1998, ApJ, 504, L57
Eisenstein, D.J., 2003, in ASP Conference Series, volume 280, Next Generation Wide Field Multi-Object Spectroscopy, ed. M.J.I. Brown & A. Dey (ASP: San Francisco) pp. 35-43; astro-ph/0301623
Eisenstein, D. J., et al. 2005, ApJ, 633, 560
Eisenstein, D. J., Seo, H.-J., & White, M. 2007, ApJ, 664, 660
Feldman, H. A., Kaiser, N., Peacock, J. A. 1994, ApJ, 426, 23
Guzik, J., & Seljak, U. 2002, MNRAS, 335, 311
Hamilton, A. J. S. 1993, ApJ, 417, 19
Hamilton, A. J. S. 1998, in The Evolving Universe, ed. D. Hamilton (Dordrecht: Kluwer), 185
Hawkins, E., et al. 2003, MNRAS, 346, 78
Heavens, A. F., & Taylor, A. N. 1995, MNRAS, 275, 483
Hewett, P. C. 1982, MNRAS, 201, 867
Holtzman, J. A. 1989, ApJS, 71, 1
Hu, W., & Haiman, Z. 2003, Phys. Rev. D, 68, 063004
Hu, W., & Sugiyama, N. 1996, ApJ, 471, 542
Hu, W., & White, M. 1996, ApJ, 471, 30
Huff, E., et al. 2007, Astroparticle Physics, 26, 351
Jain, B., & Bertschinger, E. 1994, ApJ, 431, 495
Kaiser, N. 1987, MNRAS, 227, 1
Kaiser, N., & Peacock, J. A. 1991, ApJ, 379, 482
Komatsu, E., et al. 2009, ApJS, 180, 330
Kravtsov, A. V., et al. 2004, ApJ, 609, 35
Landy, S. D., & Szalay, A. S. 1993, ApJ, 412, 64
Linder, E. V. 2003, Phys. Rev. D, 68, 083504
Ma, Z. 2007, ApJ, 665, 887
Matsubara, T. 2004, ApJ, 615, 573
Matsubara, T. 2007, Phys. Rev. D, 77, 063530
Mehta, K., et al. in prep
Meiskin, A., & White, M. 1999, MNRAS, 308, 1179
Meiksin, A., White, M., Peacock, J. A. 1999, MNRAS, 304, 851
Metchnik, M., & Pinto, P. 2010, in prep
Okumura, T., et al. 2008, ApJ, 676, 889
Padmanabhan, N., White, M., Eisenstein D.J. 2007, MNRAS, 376, 1702
Padmanabhan, N., & White, M. 2008, Phys. Rev. D, 77, 123540
Padmanabhan, N., & White, M. 2009, Phys. Rev. D, 80, 063508
Padmanabhan, N., et al. 2009, MNRAS, 397, 1862
Park, C., Gott, J. R., da Costa, L. N. 1992, ApJ, 392, L51
Peacock, J. A., & Nicholson, D. 1991, MNRAS, 253, 307
Peacock, J. A., et al. 2001, Nature, 410, 169
Peebles, P. J. E., & Yu, J. T. 1970, ApJ, 162, 815
Peebles, P. J. E. 1973, ApJ, 185, 413
Peebles, P. J. E. 1980, The Large-Scale Structure of the Universe (Princeton: Princeton University Press)
Percival, W. J., et al. 2004, MNRAS, 353, 1201
Percival, W. J., & White, M. 2009, MNRAS, 393, 29
Sanchez, A. G., Baugh, C. M., Angulo, R. 2008, 390, 1470
Scocciamarro, R., Zaldarriaga, M., Hui, L. 1999, ApJ, 527, 1
Seo, H.-J., & Eisenstein, D. J. 2003, ApJ, 598, 720
Seo, H.-J., & Eisenstein, D. J. 2005, ApJ, 633, 575
Seo, H.-J., Siegel, E. R., Eisenstein, D. J., White, M. 2008, ApJ, 686, 13
Seo, H.-J., et al. 2009, ApJ, submitted (astro-ph/0910.5005v2)
Sharp, N. A. 1979, A&A, 74, 308
Sirko, E. 2005, ApJ, 634, 728
Smith, R. E., Scoccimarro, R., Sheth, R. K. 2008, Phys. Rev. D, 77, 043525
Song, Y.-S. & Percival, W. J. 2008, Phys. Rev. D, in press (astro-ph/0807.0810)
Sunyaev, R. A., & Zeldovich, Y. B. 1970, Ap&SS, 7, 3
Szalay, A. S., Matsubara, T., Landy, S. D. 1998, ApJ, 498, L1
Szapudi, I. 2004, ApJ, 614, 51
Tegmark, M., et al. 2006, Phys. Rev. D, 74, 123507
Tegmark, M., Hamilton, A. J. S., Xu, Y. 2002, MNRAS, 335, 887
White, M., Song, Y.-S., Percival, W. J. 2009, MNRAS, 397, 1348
Zaroubi, S. & Hoffman, Y. 1995, ApJ, 449, 446
Zehavi, I., et al. 2002, ApJ, 571, 172
Zheng, Z., et al. 2005, ApJ, 633, 791

TABLE 1
HOD PROPERTIES

Model	Total # of Galaxies[1]	Satellite Fraction (%)	M_{cen} ($h^{-1}M_{\odot}$)	M_{sat} ($h^{-1}M_{\odot}$)	$\bar{n}$ [2] (h^3 Mpc^{-3})	$\bar{n}P_{0.2}$	$\aleph_{nonlin}$
DM	4×10^6	-	-	-	0.004	4.60	0.0
HOD1	2×10^6	5	1.4×10^{12}	9.2×10^{13}	0.002	5.78	450.0
HOD2	1×10^6	5	2.6×10^{12}	1.5×10^{14}	0.001	3.59	700.0
HOD3	3×10^5	5	6.4×10^{12}	3.1×10^{14}	0.0003	1.59	1550.0

NOTE. — HODs are referred to by the designations under the "Model" heading throughout the paper.

[a]Number of DM particles in the DM only case.
[b]The nominal Poisson shot-noise is $\bar{n}^{-1}$.

TABLE 2
FIT RESULTS FOR EACH HOD MODEL

Model	$\alpha - 1$ (%)	σ_α (%)	Σ_{nl}	r_{scale}	χ^2 (per d.o.f)	bias [1] (b)	σ_8
DM	0.0457	0.0023	6.66	19.99	0.95	1.25	0.63
HOD1	0.1065	0.2243	5.61	19.78	0.97	2.04	1.11
HOD2	0.1634	0.2449	5.85	19.98	0.89	2.28	1.25
HOD3	0.4897	0.3326	6.27	20.04	0.75	2.77	1.55

NOTE. — Fitting range: $30 \leq r_s \leq 200h^{-1}$ Mpc. σ_α is the error on the mean α of the 44 simulations.

[a]Bias is not equal to 1 for the DM only case because we are working in redshift space.

TABLE 3
DIFFERENCE IN MEAN α BETWEEN $\omega_0(r_s)$ AND $P(k)$

Model	$\Delta\alpha_{\omega P}$ (%)
DM	0.0516 ± 0.1205
HOD1	0.0076 ± 0.0672
HOD2	0.0205 ± 0.0600
HOD3	0.1035 ± 0.0665

APPENDIX
EVALUATING $\widetilde{W}_\ell(K)$

The expressions for $\widetilde{W}_\ell(k)$, in terms of polynomials of k times trigonometric functions, involve a lot of cancellation. This makes them unstable to direct evaluation. However if we define

$$K_n(k) = \frac{2+n}{(kr_s)^{2+n}} \int_0^{kr_s} x^n \sin x \; dx \tag{A1}$$

then

$$\widetilde{W}_0(k) = \frac{8\pi}{3} \left[\frac{1}{3} \left(K_7 - K_{16} \right) - \left(K_{10} - K_{13} \right) \right] \tag{A2}$$

while

$$\widetilde{W}_2(k) = -\frac{24\pi}{5k^2} \left[3K_5 - 16K_8 + 25K_{11} - 12K_{14} \right]. \tag{A3}$$

It is straightforward to evaluate $K_n(x)$, the limits are

$$K_n(x) = 1 - \frac{n+2}{3!(n+4)} x^2 + \frac{n+2}{5!(n+6)} x^4 + \cdots \tag{A4}$$

as $x \to 0$ and

$$K_n(x) = -(n+2)\frac{\cos x}{x^2} + n(n+2)\frac{\sin x}{x^3} + \cdots \tag{A5}$$

as $x \to \infty$. The K_n also satisfy a simple recurrence relation

$$K_n(x) = \frac{n+2}{x^3} \left[n \sin x - x \cos x - (n-1) x K_{n-2} \right]. \tag{A6}$$

Use of this recurrence relation for high k and the power-series expansion for low k results in stable evaluation of the $\widetilde{W}_\ell$.